# Combustion modeling study for a GOX-GCH4 multi-element combustion chamber

**By H. Terashima† AND Y. Daimon‡**

Faculty of Engineering, Hokkaido University
N13 W8, Kita-ku, Sapporo, Hokkaido 060-8628, Japan

The present study investigates the effect of recess length on $CH_4/O_2$ combustion flow field of a rocket injector using the compressible Navier-Stoke equations with a skeletal reaction mechanism. The recess length parametrically changes with four different lengths, while the other geometrical parameters are fixed. The results with recessed injectors are compared to those with a non-recessed injector. A main difference of combustion flow fields between the non-recessed and recessed injectors lies in the interaction mechanism of a large recirculation flow in the corner of combustion chamber with the incoming $CH_4$ jet and flame anchoring region behind the post, which indicates that a stable flame anchoring and combustion can be achieved with recessed injectors. With increasing the recess length, the combustion in the recessed region is more promoted, resulting in the earlier formation of higher-temperature combustion gas regions in the combustion chamber. However, the temperature increase in the combustion chamber is saturated with a longer recess length because no significant change of combustion happens in the recessed region due to the complete consumption of the incoming $CH_4$. On the other hand, the influence of the combustion gas on the $CH_4$ upper and lower walls becomes larger with increasing the recess length due to the formation of larger amount of combustion gases.

## 1. Introduction

Recessed injectors have been widely used in the design of injector elements for liquid rocket engines since some preferable performance such as increasing combustion efficiency or reducing the risk of combustion instabilities may be achieved with an appropriated recess length. An experimental study [1] investigated the effect of a recessed injector on flame stabilization using an optically accessible sub-scale rocket combustor. The study presented that a recessed injector significantly increases the flame expansion shortly after injection and the pressure drop in the recessed region increases strongly compared to a non-recessed injector. In addition, the study observed that a smaller combustion roughness is generally achieved with a recessed injector. However, the experiment was only conducted with a single recessed injector geometry, which may bring some uncertainty for understanding the effect of recessed injector, e.g., the effect of a recess length, on combustion characteristics. Further, due to the limitation of optical access into the recessed region, less information are available for detailed combustion flow fields such as spatial temperature or chemical species distributions.

† Corresponding author, htera@eng.hokudai.ac.jp
‡ daimon.yu@jaxa.jp, Japan Aerospace Exploration Agency (JAXA), Japan

Recently, a numerical study in a context of Reynolds-averaged Navier-Stokes simulations (RANS) was performed for a single-element combustion chamber with various recess lengths [2] in comparison with an experiment [3]. The computational result showed that the experimental trends of the wall heat flux and wall pressure distributions are simulated well for moderate recess lengths. However, the prediction unfortunately failed with increasing recess lengths, in which the pressure increase in the combustion chamber of the experiment cannot be simulated by the RANS simulation. The study suggested that the disagreement may come from a fact that the combustion phenomena in the recessed region cannot be captured properly by the RANS simulation due to the lack of unsteady flow features. Thus, it was concluded that resolving unsteady combustion phenomena in the recessed region may be a key for accurately predicting the experimental trend.

The aim of the present study is to numerically investigate the effect of recess length on combustion flow fields of a recessed injector element. The present study applies a two-dimensional (2-D) direct numerical simulation in order to address detailed combustion flow fields with resolving unsteady flow features in the recessed region, which include a significant interaction between flow and chemical reaction. The recess length parametrically changes to obtain the effect of recess length on combustion flow fields. A 2-D simulation is used here for properly resolving the combustion flow fields with affordable grid points and computational times, while a discussion on the combustion performance such as efficiency is difficult to be achieved.

## 2. Numerical method

### 2.1. *Governing equations*

The governing equations are the two-dimensional compressible Navier-Stokes equations with the mass conservation equations of each chemical species in a curvilinear coordinate system and a thermally perfect gas is assumed, which are written as follows:

$$\frac{\partial \rho}{\partial t} + \nabla \cdot (\rho u) = 0, \tag{2.1}$$

$$\frac{\partial (\rho u)}{\partial t} + \nabla \cdot (\rho u \otimes u + p\delta - \tau) = 0, \tag{2.2}$$

$$\frac{\partial E}{\partial t} + \nabla \cdot [(E + p)u - \tau \cdot u + q] = 0, \tag{2.3}$$

$$\frac{\partial (\rho Y_s)}{\partial t} + \nabla \cdot (\rho Y_s u - \rho D_s \nabla Y_s) = \dot{\omega}_s, \tag{2.4}$$

$$p = \rho R \sum_{s=1}^{N} \frac{Y_s}{M_s} T, \tag{2.5}$$

where $\rho$ is the density, $u$ is the velocity vector, $p$ is the pressure, $\delta$ is the unit tensor, $\tau$ is the viscous stress tensor, $E$ is the total energy ($E = \rho e + \frac{1}{2}\rho u \cdot u$), $q$ is the heat flux vector, $e$ is the internal energy, $Y_s$ is the mass fraction, $D_s$ is the diffusion coefficient, $\dot{\omega}_s$ is the production rate of each species $s$. $R$ is the universal gas constant ($R = 8.314$ J mol$^{-1}$ K$^{-1}$), $T$ is the temperature, and $M_s$ is the molar mass of each species. Here the subscript $s = 1 \sim N$ where $N$ is the total number of species.

The single component viscosities and binary diffusion coefficients are calculated by the standard kinetic theory expression of Hirschfelder [4], and the single component thermal conductivities are calculated by Warnatz's model [5]. For mixtures, the thermal conductivity is modeled with the formula of Mathur et al. [6], and analogous to the thermal conductivity, the mixture-averaged viscosity is purposely modeled with an empirical approximation [7] for the low computational cost. The mixture diffusion coefficient $D_s$ is given by a mixture-averaged model based on Fick's Law [8, 9]. The Dufour effect for the heat flux, the Soret effect and the pressure diffusion for the diffusion flux are neglected in this study.

The fluid and chemical reaction parts in the governing equations are solved separately in temporal direction. The fluid parts in Eqs. (2.1) – (2.4) are integrated under the assumption that the chemical reactions are frozen, $\dot{\omega}_s = 0$ in Eq. (2.4), whereas the chemical reaction parts are treated under the assumption that the volume and internal energy of fluids are constant. Thus, the governing equations for the chemical reactions are derived as follows:

$$\rho \frac{\mathrm{d}Y_s}{\mathrm{d}t} = \dot{\omega}_s, \tag{2.6}$$

$$\rho c_v \frac{\mathrm{d}T}{\mathrm{d}t} = -\sum_{s=1}^{N} e_s \dot{\omega}_s, \tag{2.7}$$

where $e_s$ is the internal energy of each species and $c_v$ is the specific heats at a constant volume for mixture. The spatial derivatives in Eqs. (2.1) – (2.4) are neglected in the chemical reaction part.

CHEMKIN-II libraries [10, 11] are used to evaluate the variables related to thermodynamics, transports, and chemical reactions. Primitive variables such as the temperature, mass fractions, and pressure are exchanged between the fluid equations (2.1) – (2.4) and the chemical reaction equations (2.6) and (2.7) at each time step.

### 2.2. *Fluid part*

For the Navier–Stokes equations without chemical reaction terms, the numerical flux is evaluated using the Harten–Lax–van Leer–Contact scheme [12] with a modification [13]. Higher-order spatial accuracy is achieved using the Monotone Upstream Centered Schemes for Conservation Law with primitive variable interpolation and a minmod limiter [14]. Velocity reconstruction by Thornber et al. [15] is applied to the reduce numerical dissipation introduced by low Mach number features. The viscous, heat conductivity, and diffusion terms are evaluated by the second-order central differencing. The time integration is performed with the third-order total variation diminishing Runge–Kutta scheme [16]. In this study, no sub-grid scale model is used, i.e., the interactions between the fluid and chemical reaction are expected to be resolved properly with computational grids.

### 2.3. *Chemical reaction part*

A robust and fast explicit time integration method [17] is used to efficiently conduct the time integration of the reaction equations (2.6) and (2.7) while overcoming possible stiffness. The method is based on a quasi-steady-state assumption and a general formula that preserves conservation laws for any integration operator. The performance and accuracy have been comprehensively validated with zero-dimensional ignition problems under a wide range of conditions [17]. These numerical techniques have been successfully applied to various compressible reactive flow simulations [18–20].

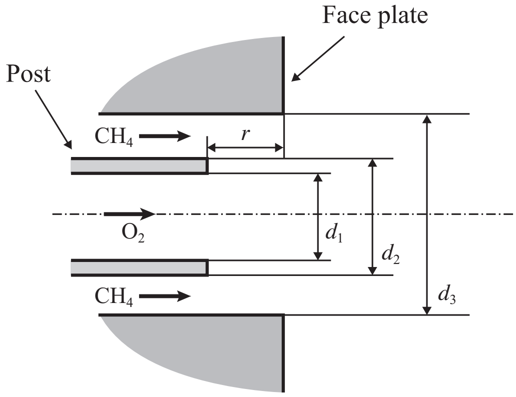


FIGURE 1. Schematic of a recessed injector.

TABLE 1. Dimensions for recessed injectors.

| | mm |
|---|---|
| GOX internal diameter, $d_1$ | 4 |
| $GCH_4$ internal diameter, $d_2$ | 5 |
| $GCH_4$ external diameter, $d_3$ | 6 |
| GOX post wall thickness | 0.5 |
| Recessed length, $r$ | 0, 3, 6, 9, 12 |

## 3. Computational conditions

In this study, a two-dimensional (2-D) domain without an engine nozzle and injector tube is considered for simplicity. As shown in Fig. 1, gaseous oxygen is injected from the inner tube, which is surrounded by gaseous methane injected from the outer tube. The distance between the post and face place, denoted by $r$, is defined as the recess length. Table. 1 presents the dimensions for the recessed injector shown in Fig. 1. The present study parametrically changes the recess length from 0 to 12 mm, while the other geometrical parameters are fixed. Hereafter, each injector is denoted as R0 (non-recessed injector), R3, R6, R9, and R12 for brevity. The size of combustion chamber is 250 mm $\times$ 12 mm.

Figure 2 shows a computational grid for modeling combustion flow fields in the recessed injector and combustion chamber, where a grid for the recess length of $r = 9$ mm, R9, is presented as an example. The number of grid points for R9 is $1157 \times 403$, which depends on the recess length, e.g., the grid for R0 consists of $498 \times 403$ points. The minimum grid size is $\Delta s = 1.0$ $\mu$m to resolve the boundary layer profiles near the walls. The post height is resolved with 60 grid points. Note that a grid convergence study preliminarily conducted for a non-recessed injector case with four different grid resolutions demonstrates that the present grid resolution is sufficient for resolving combustion

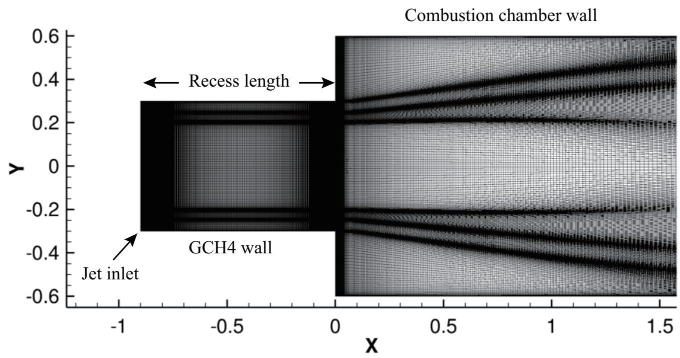


FIGURE 2. Computational grid for R9.

flow features such as methane/oxygen non-premixed flame dynamics discussed in the following section. Since a single rectangular domain is used, an immersed boundary technique is applied in order to handle the grid points inside the wall (see the upper-left and lower-left regions in Fig. 2).

The injection conditions are presented in Table. 2. The injection velocity is determined from a preliminary result using a RANS simulation, in which the complete 3-D geometry of the injector and chamber is simulated. The chamber pressure is set to 2.0 MPa as a target combustion pressure and the injection temperature is 300 K for both jets. Thus, three key parameters are determined as in Table. 3. While similar values to 3-D or experiment hold for the velocity and momentum flux ratios, the mixture ratio O/F ends up with a very large and unrealistic value due to the 2-D geometry assumption. Therefore, the combustion performance of this injector and chamber would not be discussed.

The initial velocity profile at the inlet is obtained with the 1/7th power law. At the jet inlet, the pressure is extrapolated from an interior point while the temperature and mass fractions are specified with the initial values. The constant mass flow rate is enforced and therefore the velocity profile at the inlet may change during the computation. All the domains is initially assumed to be filled with the equilibrium gas, which is determined using NASA-CEA2 [21] with a stoichiometric condition for methane/oxygen and a temperature of $300$ K at constant pressure and enthalpy. The high-temperature equilibrium gas initiates the ignition of methane/oxygen jets injected into the chamber. An adiabatic wall is assumed with a non-slip velocity condition for the inlet, $CH_4$ side wall, and combustion chamber wall. A non-reflecting boundary condition [22,23] with a mean pressure of $2.0$ MPa is applied to the outlet boundary.

The Courant-Friedrichs-Lewy (CFL) number is set to $0.8$, which corresponds to a physical time step size of approximately $\Delta t = 5 \times 10^{-10}$ s. A reaction mechanism of methane proposed by DLR, which consists of $21$ species and $97$ reactions, is used for calculating the reaction rate in Eq. (2.4).

## 4. Results

### 4.1. *Unsteady combustion flow fields*

Figure 3 shows instantaneous combustion flow fields with the temperature and mass fractions of $CH_4$ in comparisons between R0 and R9. In both cases, non-premixed flames are generated between $CH_4$ and $O_2$ jets which are initiated by the high-temperature

TABLE 2. Injection conditions.

| | $p$, MPa | $T$, K | $u$, m/s |
|---|---|---|---|
| GOX for inner jet | 2 | 300 | 150 |
| $GCH_4$ for outer jet | 2 | 300 | 170 |

TABLE 3. Injection parameters, where a reference area $A$ is calculated using the jet height with an assumption of the unit span. A symbol $J$ is the momentum flux ratio and O/F is the mixture ratio.

| $J = \frac{(\rho uu)_{CH_4}}{(\rho uu)_{O_2}}$ | $\bar{V} = \frac{u_{CH_4}}{u_{O_2}}$ | O/F$= \frac{(\rho uA)_{CH_4}}{(\rho uA)_{O_2}}$ |
|---|---|---|
| 0.64 | 1.13 | 7.06 |

equilibrium gas initially occupied in the combustion chamber. A flame anchoring is achieved in the region behind the post, where a small recirculation flow field is established and hence sufficient amounts of fresh $CH_4$ and $O_2$ are steadily supplied. Two large recirculation regions are formed in the upper and lower corners in the combustion chamber, where some amounts of combustion gases and unburnt $CH_4$ are captured and thus a high-temperature gas recirculation region is established. Strong unsteadiness is only observed in the recessed region and the corner region of the combustion chamber, while high-temperature burnt gases steadily flow through in the downstream region.

A main difference between R0 and R9 can be observed in the interaction between the large recirculation flow in the corner of combustion chamber and the flame anchoring region behind the post. For R0, the large recirculation flow directly interferes the incoming $CH_4$ jet and the flame anchoring flow region behind the post, whereas no interferences exit for R9 simply due to the recessed geometry. Thus, the result may indicate that the non-premixed flame can be stably generated in the case of recessed injector because of no external disturbances compared to non-recessed injector. Since the large amount of high-temperature combustion gases is produced in the recessed region, the temperature in the corner of the combustion chamber becomes apparently higher along with lower mass fraction of $CH_4$ in the case of R9 as shown in Fig. 3. Therefore, the present result demonstrates that there are significant differences of the combustion flow fields such as temperature or chemical species distributions near the face plate between non-recessed and recessed injectors. No significant differences are found in the qualitative flow features among the recessed injectors.

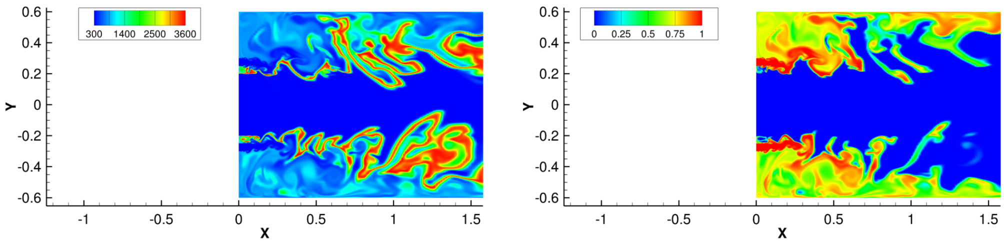


(a) R0: non-recessed injector

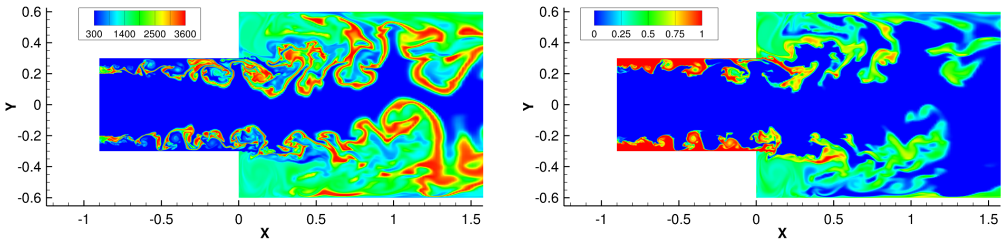


(b) R9: recess length of 9 mm

FIGURE 3. Comparison of instantaneous combustion flow fields at approximately $t = 1.138$ ms from the injection. Left: temperature, right: mass fraction of $CH_4$

### 4.2. *Comparison of mean flow fields*

Figure 4 shows a comparison of mean temperature distributions and streamlines among all the injectors. As mentioned above, it is also confirmed with the mean flow field that the large recirculation flow region is generated in the corner of combustion chamber for all the cases, while no significant differences are observed for the size of recirculation flow region. For R0, the recirculation region is formed close to the flame anchoring region behind the post, indicating that a stronger interaction occurs between the two regions compared to the recessed injectors. With increasing the recess length, since larger amounts of combustion gases are produced in the recessed region, higher-temperature gas regions are eventually formed in the chamber region near the face plate. In the combustion chamber, it looks like the flame, the high-temperature region above 2000 K, expands largely with the recessed injectors compared to the non-recessed one, which is a consistent trend with the past experimental observation [1].

It is also found that the injected $O_2$ is consumed earlier with increasing the recess length. For fair and quantitative comparison, Fig. 5 shows a comparison of a jet potential core length from the post, which is defined with a position where the value of 90% mass fraction of $O_2$ is observed on the ceternline. In the case of recessed injectors, the potential core length linearly decrease with increasing the recess length because the combustion in the recessed region is more promoted with increasing the recess length. However, the potential core length with R12 shows a different trend, providing a similar value to R9. This fact may indicate that the combustion is almost completed in the recessed region with R9 and R12.

Thus, the mean distribution of mass fraction of $CH_4$ for the recessed injector is presented in Fig. 6. In shorter recess lengths such as R3 and R6, certain amounts of $CH_4$

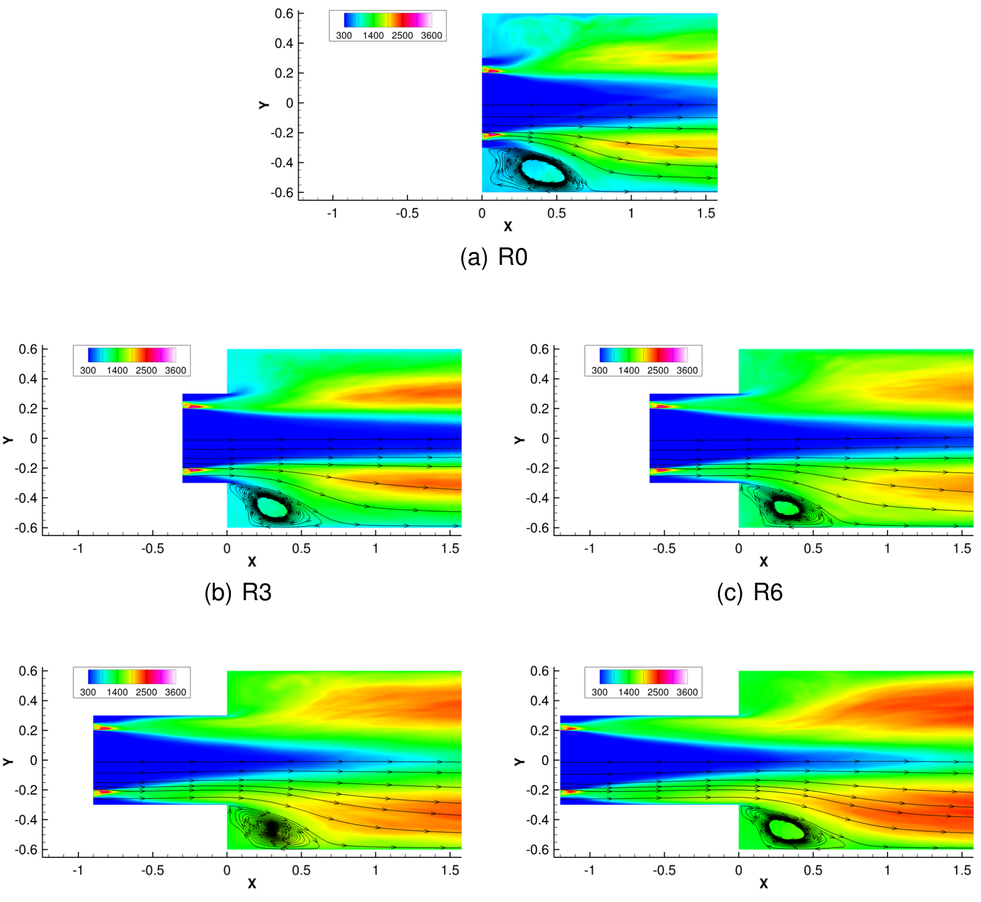


(a) R0 (b) R3 (c) R6 (d) R9 (e) R12

FIGURE 4. Comparison of mean temperature distributions.

are supplied into the combustion chamber with the generation of relatively large $CH_4$ fraction region in the corners, whereas less $CH_4$ exit in the combustion chamber with R9 and R12 because of a complete combustion achieved in the recessed region. Thus, the combustion flow field may not change with further increase of recess length, suggesting that some effects of recess length may be saturated with a certain recess length. On the other hand, the RANS simulation [2] showed that large amount of $CH_4$ is still injected to the combustion chamber even with a very long recess length of 21 mm, which may be one of the reasons that the RANS fails to capture the experimental trend [3] against the recess length.

Figure 7 shows the temperature profiles on the wall. The x coordinate means the distance from the jet inlet along the $CH_4$ upper wall (until 0 cm), the face plate wall (from 0 to 0.3 mm), and the combustion chamber wall. It is found that, with increasing the recess length, the combustion gas interacts with the $CH_4$ upper and lower walls due to the consumption of low-temperature fresh $CH_4$ jet, resulting in a significant increase of wall temperature. The region where the wall temperature increases becomes larger

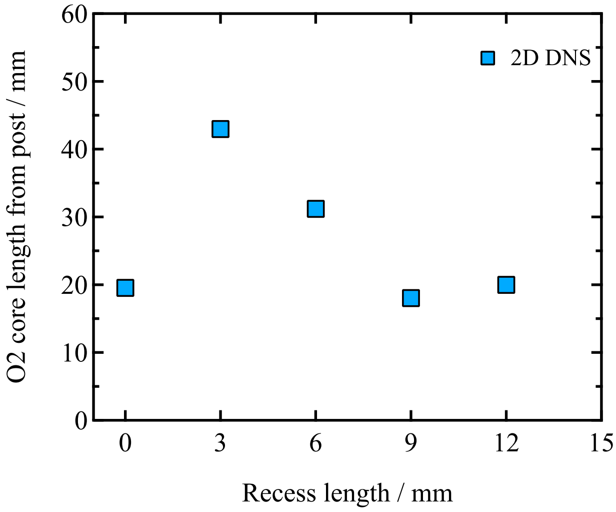


FIGURE 5. Comparison of potential core length of $O_2$ jet.

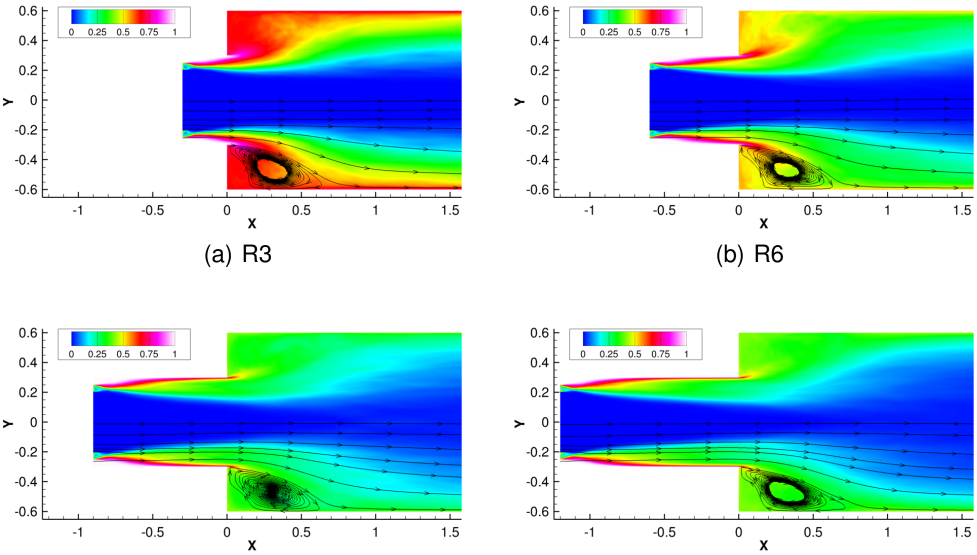

(a) R3

(b) R6

(c) R9

(d) R12

FIGURE 6. Comparison of mean mass fraction of $CH_4$ distributions.

with increasing the recess length, which may be an important fact on heat protection of injector wall. In the combustion chamber, the wall temperature gradually increases with increasing the recess length, since some amounts of higher-temperature combustion gases are supplied in the corner region of the combustion chamber. However, no further temperature increase is observed with R12 due to the complete combustion in the recessed region, which is a consistent result with the $O_2$ jet potential core shown in Fig. 5. Therefore, no significant changes of combustion flow fields by increasing the recess

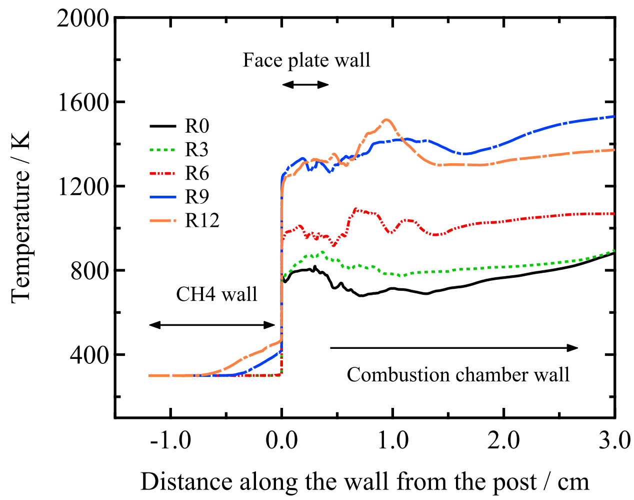


FIGURE 7. Comparison of wall temperature distributions in a coordinate along the wall.

length would be expected. The present result may suggest that a limitation exists for the effect of recess length on combustion flow fields and thus combustion performance, providing that a key lies in the combustion behavior in the recessed region. Further studies on the effect of recess length would be required for the connection between the combustion flow fields and combustion effciency.

## 5. Conclusions

A 2-D DNS simulation with a skeletal reaction mechanism has been performed for a $CH_4/O_2$ injector in order to investigate the effect of recess length on the combustion flow field, where four recess lengths with a non-recessed injector are parametrically compared. A main difference between non-recessed and recessed injectors lies in the interference of large recirculation flow to the incoming $CH_4$ jet and the flame anchoring region behind the post, indicating that stable combustion is highly possible with recessed injectors. With increasing the recess length, the combustion in the recessed region is more promoted, resulting in the earlier formation of higher-temperature combustion gas regions in the combustion chamber. However, the temperature increase in the combustion chamber is saturated with the recess lengths with R9 and R12 because of the complete combustion in the recessed region, indicating that no further changes of the combustion flow field are expected with longer recess length. On the other hand, the influence of the combustion gas on the $CH_4$ upper and lower walls becomes larger with increasing the recess length.

## Acknowledgments

Financial support has been provided by the German Research Foundation (Deutsche Forschungsgemeinschaft – DFG) in the framework of the Sonderforschungsbereich Transregio 40.

## References

[1] LUX, J. AND HAIDN, O. (2009). Effect of recess in high-pressure liquid oxygen/methane coaxial injection and combustion. *Journal of Propulsion and Power*, **25**(1), 24–32.

[2] DAIMON, Y., TERASHIMA, H., TANI, H. AND NEGISHI, H. (2017). Numerical investigation on effects of recess variation upon a gch4/gox shear coaxial combustion chamber. In: *Proceedings of 31st International Symposium on Space Technology and Science (ISTS)*.

[3] SILVESTRI, S. (2016). Experimental and numerical investigation on recess variation of a shear coax injector in a GOX-GCH4 combustion chamber. In: *Proceedings of Space Propulsion 2016*.

[4] HIRSCHFELDER, J., CURTISS, C. AND BIRD, R. (1954). *Molecular theory of gases and liquids*. John Wiley and Sons, Inc., New York.

[5] PETERS, N. AND WARNATZ, J. (1982). *Numerical methods in laminar flame propagation: A GAMM-Workshop*, vol. 6. Informatica International, Inc.

[6] MATHUR, S., TONDON, P. AND SAXENA, S. (1967). Thermal conductivity of binary, ternary and quaternary mixtures of rare gases. *Molecular Physics*, **12**(6), 569–579.

[7] WARNATZ, J., MAAS, U. AND DIBBLE, R.W. (2006). *Combustion: physical and chemical fundamentals, modeling and simulation, experiments, pollutant formation*. Springer.

[8] BIRD, R.B., STEWART, W.E. AND LIGHTFOOT, E.N. (1960). *Transport phenomena*, vol. 2. Wiley New York.

[9] SUTTON, K. AND GNOFFO, P.A. (1998). Multi-component diffusion with application to computational aerothermodynamics. In: *Proceedings of 7th AIAA/ASME Joint Thermophysics and Heat Transfer Conference, AIAA98-2575*.

[10] KEE, R., RUPLY, F. AND MILLER, J. (1989). Chemkin-II: A fortran chemical kinetics package for the analysis of gas-phase chemical kinetics. *Sandia Report SAND89-8009 (1989)*.

[11] KEE, R., DIXON-LEWIS, G., WARNATZ, J., COLTRIN, M. AND MILLER, J. (1986). A fortran computer code package for the evaluation of gas-phase, multicomponent transport properties. *SAND86-8246 (1986)*.

[12] TORO, E.F., SPRUCE, M. AND SPEARES, W. (1994). Restoration of the contact surface in the HLL-Riemann solver. *Shock Waves*, **4**(1), 25–34.

[13] KIM, S.D., LEE, B.J., LEE, H.J. AND JEUNG, I.S. (2009). Robust HLLC Riemann solver with weighted average flux scheme for strong shock. *Journal of Computational Physics*, **228**(20), 7634–7642.

[14] VAN LEER, B. (1997). *Flux-vector splitting for the Euler equation*. Springer.

[15] THORNBER, B., MOSEDALE, A., DRIKAKIS, D., YOUNGS, D. AND WILLIAMS, R.J. (2008). An improved reconstruction method for compressible flows with low mach number features. *Journal of Computational Physics*, **227**(10), 4873–4894.

[16] GOTTLIEB, S. AND SHU, C.W. (1998). Total variation diminishing Runge-Kutta schemes. *Mathematics of Computation of the American Mathematical Society*, **67**(221), 73–85.

[17] MORII, Y., TERASHIMA, H., KOSHI, M., SHIMIZU, T. AND SHIMA, E. (2016). ERENA: A fast and robust jacobian-free integration method for ordinary differential equations of chemical kinetics. *Journal of Computational Physics*, **322**, 547–558.

[18] TERASHIMA, H., KOSHI, M., MIWADA, C., MOGI, T. AND DOBASHI, R. (2014).

Effects of initial diaphragm shape on spontaneous ignition of high-pressure hydrogen in a two-dimensional duct. *International Journal of Hydrogen Energy*, **39**(11), 6013–6023.

[19] TANI, H., TERASHIMA, H., KOSHI, M. AND DAIMON, Y. (2015). Hypergolic ignition and flame structures of hydrazine/nitrogen tetroxide co-flowing plane jets. *Proceedings of the Combustion Institute*, **35**(2), 2199–2206.

[20] TERASHIMA, H. AND KOSHI, M. (2015). Mechanisms of strong pressure wave generation in end-gas autoignition during knocking combustion. *Combustion and Flame*, **162**(5), 1944–1956.

[21] MCBRIDE, B.J. AND GORDON, S. (1996). Computer program for calculation of complex chemical equilibrium compositions and applications: II. users manual and program description. *NASA reference publication*, **1311**, 84–85.

[22] THOMPSON, K.W. (1987). Time dependent boundary conditions for hyperbolic systems. *Journal of Computational Physics*, **68**(1), 1–24.

[23] RUDY, D.H. AND STRIKWERDA, J.C. (1980). A nonreflecting outflow boundary condition for subsonic navier-stokes calculations. *Journal of Computational Physics*, **36**(1), 55–70.